Visualizing Magnetic Structure in 3D Nanoscale Ni–Fe Gyroid Networks

Llandro, J.; Love, D. M.; Kovács, A.; Caron, J.; Vyas, K. N.; Kakay, A.; Salikhov, R.; Lenz, K.; Faßbender, J.; Scherer, M. R. J.; Cimorra, C.; Steiner, U.; Barnes, C. H. W.; Dunin-Borkowski, R. E.; Fukami, S.; Ohno, H.;

Originally published:

April 2020

Nano Letters 20(2020)5, 3642-3650

DOI: https://doi.org/10.1021/acs.nanolett.0c00578

Visualizing Magnetic Structure in 3D Nanoscale Ni-Fe Gyroid Networks

Justin Llandro[1,2,3], David M. Love[4], András Kovács[5], Jan Caron[5], Kunal N. Vyas[4]‡, Attila Kákay[6], Ruslan Salikhov[6], Kilian Lenz[6], Jürgen Fassbender[6,7], Maik R. J. Scherer[4]§, Christian Cimorra[4], Ullrich Steiner[8], Crispin H. W. Barnes[4], Rafal E. Dunin-Borkowski[5], Shunsuke Fukami[1,2,3,9,10] and Hideo Ohno[1,2,3,9,10].*

AUTHOR ADDRESS [1]Laboratory for Nanoelectronics and Spintronics, Research Institute of Electrical Communication, Tohoku University, 2-1-1 Katahira, Aoba-ku, Sendai 980-8577, Japan.

[2]Center for Spintronics Research Network, Tohoku University, 2-1-1 Katahira, Aoba-ku, Sendai 980-8577, Japan.

[3]Center for Science and Innovation in Spintronics, Tohoku University, 2-1-1 Katahira, Aoba-ku, Sendai 980-8577, Japan.

[4]Cavendish Laboratory, University of Cambridge, J.J. Thomson Avenue, Cambridge CB3 0HE, United Kingdom.

[5]Ernst Ruska-Centre for Microscopy and Spectroscopy with Electrons and Peter Grünberg Institute, Forschungszentrum Jülich, 52425 Jülich, Germany.

[6]Helmholtz-Zentrum Dresden - Rossendorf (HZDR), Bautzner Landstrasse 400, 01328 Dresden, Germany.

[7]Technische Universität Dresden, Haeckelstrasse 3, 01069 Dresden, Germany.

[8]Adolphe Merkle Institute, Chemin des Verdiers 4, 1700 Fribourg, Switzerland.

[9]Center for Innovative Integrated Electronic Systems, Tohoku University, 468-1 Aramaki Aza Aoba, Aoba-ku, Sendai 980-0845 Japan.

[10]WPI Advanced Institute for Materials Research, Tohoku University, 2-1-1 Katahira, Aoba-ku, Sendai 980-8577, Japan.

KEYWORDS magnetic metamaterials, gyroids, transmission electron microscopy, off-axis electron holography

ABSTRACT Arrays of interacting 2D nanomagnets display unprecedented electromagnetic properties via collective effects, demonstrated in artificial spin ices and magnonic crystals. Progress towards 3D magnetic metamaterials is hampered by two challenges: fabricating 3D structures near intrinsic magnetic lengthscales (sub-100 nm) and visualizing their magnetic configurations. Here, we fabricate and measure nanoscale magnetic gyroids, periodic chiral networks comprised of nanowire-like struts forming 3-connected vertices. Via block co-polymer templating, we produce $Ni_{75}Fe_{25}$ single-gyroid and double-gyroid (an inversion pair of single-gyroids) nanostructures with a 42 nm unit cell and 11 nm diameter struts, comparable to the exchange length in Ni-Fe. We visualize their magnetization distributions via off-axis electron holography with sub-nm spatial resolution and interpret the patterns using finite-element

micromagnetic simulations. Our results suggest an intricate, frustrated remanent state which is ferromagnetic but without a unique equilibrium configuration, opening new possibilities for collective phenomena in magnetism, including 3D magnonic crystals and unconventional computing.

Artificial lattices (2D metasurfaces and 3D metamaterials) can manifest unprecedented properties due to the control they offer over material parameters, via tailoring both the lattice units and the interactions between them. Fully-connected 3D networks offer particularly rich prospects for new topological phenomena, extending interactions and collective effects into all three spatial dimensions, and also allowing emergent chiral effects tunable by the shape of the 3D lattice unit.

A particularly interesting example is the gyroid, a fully connected network periodic in all three dimensions notable for being entirely composed of chiral triple junctions.[1–3] Chitin gyroids with unit cells several hundred nanometers across were discovered to act as photonic crystals in biological systems,[4–8] inspiring intense research into the fabrication of artificial gyroids,[9–20] with particular focus on optical effects arising from their periodicity and chirality.

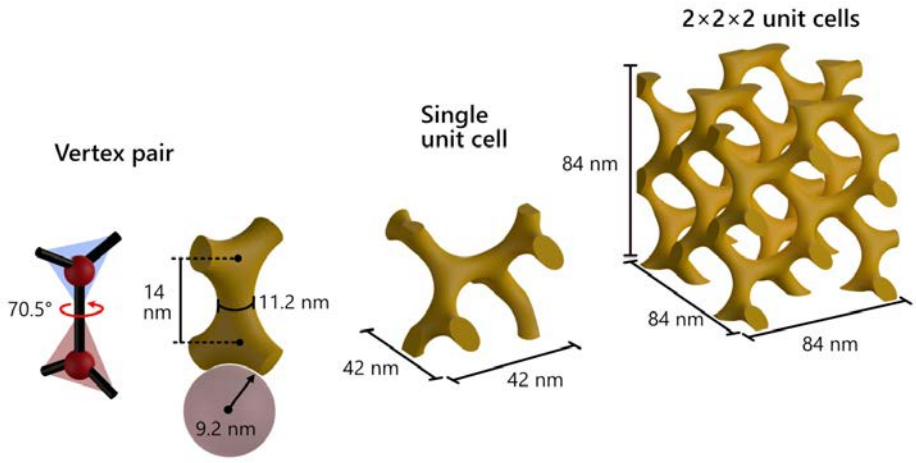

Figure 1. Structural units and symmetries of the single-gyroid network. Schematics (left to right) show a single vertex pair and a ball-and-stick model highlighting the vertices (red spheres) and the chiral twist angle of $\cos^{-1}(1/3) \approx 70.5°$, a single cubic unit cell and 2×2×2 unit cells of the single-gyroid network with volume fraction 20%, oriented with the [110] direction along the virtual substrate normal. Dimensions (strut diameter, vertex spacing, radii of curvature, unit cell edge length) are typical for the gyroid networks studied in this work. To improve clarity, the vertex pair and the single unit cell have been magnified relative to the 2×2×2 block of unit cells by factors of 2 and 1.3, respectively.

Dielectric and noble metal gyroids were observed to act as chiral beamsplitters,[11] photonic crystals and non-linear optical metamaterials[19,20] with ultra-fast responses.[21] These achievements were supplemented by the groundbreaking prediction[22] and discovery[23] of Weyl points and line nodes in the microwave response of a millimeter-scale machined ceramic gyroid. Known in different fields variously as the Laves net (or graph), the *srs* net and the K_4 crystal[24,25], the gyroid has a body-centered cubic unit cell containing triple-junction vertices formed from nanowire-like struts whose cross-sections transition between circular and elliptical (**Figure 1**). The three struts composing each vertex meet at 120° in the same plane; neighboring vertices share one of the struts and are offset from each other by a chiral angle of $\pm\cos^{-1}(1/3) \approx 70.5°$. This defines helices along high-symmetry directions of the unit cell and generates a honeycomb-like structure within the {111} planes. This single-gyroid network has space group $I4_132$; a double-gyroid with space group $Ia\bar{3}d$ can be formed from two interpenetrating single-gyroids which form an inversion pair with no intersections.

The chiral and topological effects already observed in gyroids suggest a new avenue of exploration for magnetism. Magnetic gyroid nanostructures with at least one dimension comparable to the exchange length are prime candidates for realizing in 3D collective phenomena such as monopole-like excitations currently only observed in 2D.[26,27] The 3D structural units of nanoscale gyroids display not only chirality, but also curvature, recently highlighted as a new route towards controllable non-collinear spin textures.[28–30] Curvature in bent and helical nanowires has been predicted to induce magnetochiral anisotropies, Cherenkov-like effects for magnons and an emergent Dzyaloshinskii-Moriya interaction (DMI),[31–34] even when no intrinsic DMI is present. This phenomenon makes gyroids perfect candidates to realize artificial magnetoelectric materials in which the geometry and magnetic states are strongly coupled.[35] Analogous effects for spin waves such as the non-linear optical transmission seen in photonic gyroids would position magnetic gyroids as highly sought-after true 3D magnonic crystals.[36] Finally, the connectivity of the struts and vertices make gyroids potential active elements in unconventional computing architectures, if they are shown to adopt a large number of energetically equivalent stable states.[37]

However, apart from measurements of the coercivity of Ni gyroid catalysts,[38] magnetic gyroids currently remain unexplored even from the point of view of their magnetostatic properties. To obtain a deep understanding of their magnetic behavior, it is necessary to go beyond techniques which report the averaged/ensemble properties of multi-domain gyroid networks and instead examine the magnetization texture and dynamics of individual gyroid nanostructures and their unit cells, vertices and struts. Spatially resolved magnetization textures in magnetic nanoparticles,[39] nanorods,[40] nanospirals[41] and skyrmions[42] have successfully been retrieved with nanometer resolution by off-axis electron holography (EH)[43,44] and Lorentz microscopy.[45] These transmission

electron microscopy (TEM)-based techniques detect quantitatively the phase shifts of coherent electron waves caused by their interaction with local magnetic fields in and around the sample.

Here, we demonstrate fabrication of magnetic gyroid nanostructures with unit cell dimensions smaller than 50 nm. Electrodeposition into block co-polymer templates produces $Ni_{75}Fe_{25}$ gyroids with 42 nm unit cells, making the diameters of their struts (11 nm) and the lattice parameters of their honeycomb-like {111} planes comparable to intrinsic length scales such as the exchange length, domain wall width and characteristic spin wave wavelengths. We measure the magnetic field distribution of both single-gyroid and double-gyroid $Ni_{75}Fe_{25}$ nanostructures by quantitative off-axis EH and interpret the images by comparison to finite-element micromagnetic simulations. Our results suggest nanoscale gyroids adopt a complex remanent state with multiple energetically equivalent magnetic configurations and frustration in 3D, with implications for the discovery of new emergent phenomena and applications such as unconventional computing and magnonics.

Gyroids with unit cells in the millimeter to sub-micron range may be successfully fabricated by top-down methods.[9–12] However, obtaining gyroid nanostructures with unit cells below 100 nm currently requires bottom-up methods,[13,14] particularly self-assembled block co-polymer templating.[15–18] Microphase separation of a co-polymer with blocks in an intermediate segregation regime produces gyroid networks of the minority polymer block in a matrix of the majority block.[46–49] Selectively dissolving the minority block creates a hollow gyroid template within the majority block matrix. If the template is assembled on a conductive surface, free-standing gyroid nanostructures can be fabricated by filling the template by electrodeposition and then dissolving the matrix, as illustrated in **Figure 2a**. In this work, we used a di-block co-polymer composed of poly(4-fluorostyrene) (PFS) and 38% poly(lactic acid) (PLA), where PFS and PLA are the majority and minority blocks, respectively.[50] Polymer films, 1–2 μm thick, were spin-coated onto

Au-coated Si or fluorine-doped tin oxide (FTO)-coated glass substrates and annealed for 20 mins at 173 °C in a vacuum oven, following procedures from previous work[50,51] described in the Supporting Information.

Figure 2b shows scanning electron microscopy (SEM) images of the multi-domain double-gyroid PFS template with around 38% porosity assembled on FTO after PLA removal. Structural domains 200–300 nm across tend to order with the same double-gyroid plane normal to the substrate, but adopt a variety of in-plane orientations rotated about the plane normal (exemplified by the three highlighted domains).

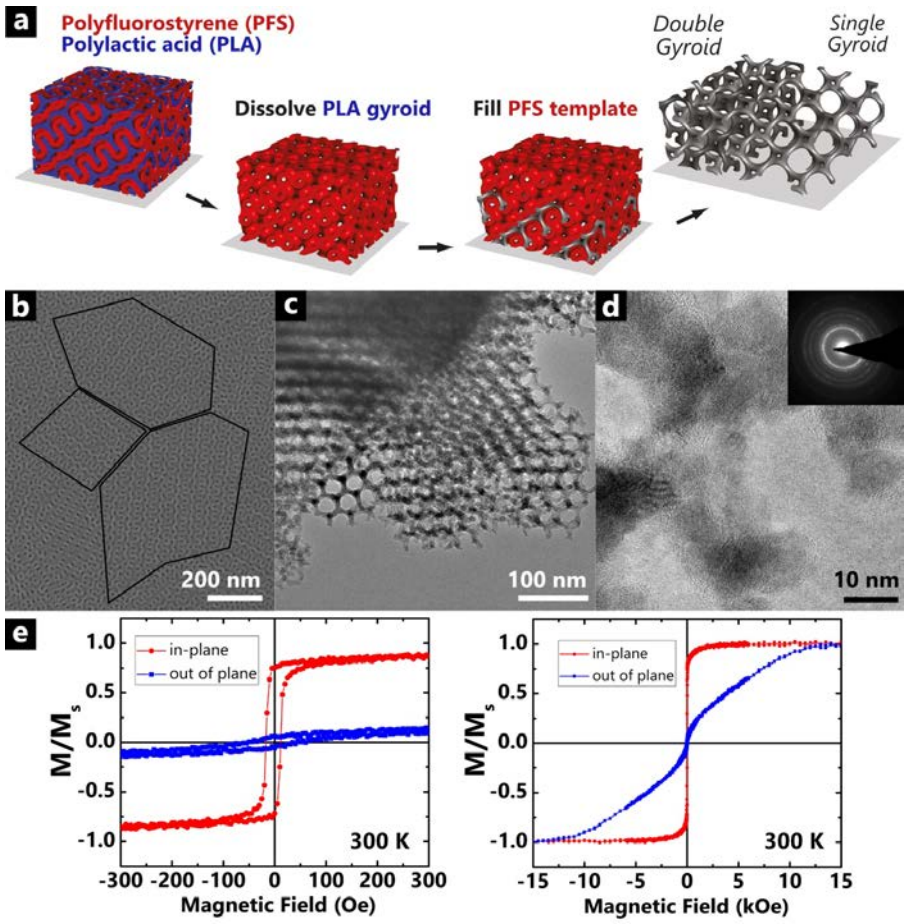

Figure 2. Fabrication and structural characterization of gyroid nanostructures. (a) Schematic of fabrication of free-standing metal gyroid nanostructures via thermal annealing of a block co-polymer template, selective dissolution of the minority block and electrodeposition, as detailed in[50] and in the Supporting Information. (b) SEM image of voided double-gyroid PFS templates showing structural domains on average around 200–300 nm across. Here, the double-gyroid's (211) face is shown consistently, but with various in-plane orientations. (c) TEM image of

lamella of free-standing Ni-Fe double-gyroids with a 42 nm unit cell and a 38% volume fraction (19% for each gyroid network) cut from gyroid films formed by Ni-Fe electrodeposition into PFS templates on fluorine-doped tin oxide (FTO)-coated glass (after PFS removal). The honeycomb-like {111} planes can be clearly seen. (d) High-resolution TEM image of Ni-Fe gyroids, showing the Ni-Fe nanocrystals which make up the struts (inset shows the selected area electron diffraction pattern). Nanocrystals are around 5 nm in size. (e) Low-field (±300 Oe) and high-field (±15 kOe) magnetic hysteresis (*M-H*) loops taken at 300 K on 1 mm diameter dot samples of Ni-Fe double-gyroids grown on Au-coated Si (gyroid film thickness 150 nm). Fields were applied in-plane and out-of-plane with respect to the substrate, showing an easy plane parallel to the substrate and an in-plane coercivity of approximately 25 Oe.

Ni-Fe was electrodeposited into the channels of the PFS gyroid templates from a mixed Ni:Fe solution held at 50°C using a conventional three-electrode potentiostat setup. The electrodeposition potential during Ni-Fe growth was chosen to lie between those of Ni and Fe in order to allow a Ni-Fe alloy close to permalloy ($Ni_{80}Fe_{20}$) to be deposited. Further details on the Ni-Fe electrodeposition are available in the Supporting Information.

Figure 2c shows TEM images of a lamella cut from a Ni-Fe gyroid film after dissolving the PFS template and **Figure 2d** shows high-resolution TEM images of a few unit cells of Ni-Fe gyroids and the selected-area electron diffraction pattern, revealing that the struts are composed of Ni-Fe nanocrystals with dimensions around 5 nm. The struts themselves are around 11.2 ± 0.5 nm in diameter and the vertex-vertex spacing is 13.8 ± 0.5 nm. The cut edge of the lamella exposes the (111) plane of a single-gyroid network, showing the unit cell to be 42 nm and the inner diameter of the honeycomb patterns to be 21.5 ± 0.5 nm. Energy-dispersive X-ray spectroscopy (EDX)

measurements of these electrodeposited Ni-Fe gyroid samples showed that the composition of the Ni-Fe is close to that of permalloy, around Ni 75% and Fe 25% (Supporting Information, **Figure S2**). The Ni-Fe gyroids' dimensions and composition invite comparison to the dipolar exchange length of permalloy (about 5 nm) and the domain wall width in 10 nm permalloy cylindrical nanowires, predicted to be around 10–15 nm.[52] This raises the possibility that the magnetization in the struts will not be completely tangential due to the curvature-induced DMI, following predictions for magnetic nano-helices where the pitch is close to the exchange length.[34] Another comparable length scale comes from exchange-dominated spin waves, which can have wavelengths of a few tens of nanometers.

Samples were also grown on Au-coated Si substrates in order to characterize the 150 nm thick multi-domain $Ni_{75}Fe_{25}$ gyroid films by vibrating sample magnetometry (VSM). For these samples, a photoresist pattern applied to the substrates confined electrodeposition to a 1 mm diameter circular dot. Magnetic hysteresis loops (**Figure 2e**) clearly show an easy plane parallel to the substrate and an in-plane coercivity of approximately 25 Oe.

To study the magnetic structure within struts and vertices of the nanoscale $Ni_{75}Fe_{25}$ gyroids, samples optimized for EH measurements were prepared on copper TEM grids coated on one side with a bi-layer of "lacey" carbon and graphene oxide films. The web-like structure of the lacey carbon allows nanostructures to be suspended between the bars of the TEM grid, reducing background and signal loss from the relatively thick, inhomogeneous metal grid. The graphene oxide helps to remove electrostatic charging and mechanical vibrations. After annealing and PLA removal as before, the PFS gyroid templates were filled with $Ni_{75}Fe_{25}$ by a two-step electrodeposition process. Firstly a higher voltage pulse was applied to seed the grid surface with a low density of $Ni_{75}Fe_{25}$ nanoparticles to provide sparse nucleation centers, followed immediately

by constant-potential growth, as described in the Supporting Information. Electron micrographs of the PFS-free samples in **Figure 3a** and **3c** show isolated gyroid nanoparticles around 150 nm across, the deliberate fabrication of which satisfies the requirement of off-axis EH of free space around the sample for the reference wave, but also allows variations in sample morphology to be studied. Because the two gyroid networks in the double-gyroid are physically separate (only coupled magnetostatically), it is possible for nanoscale local variations (e.g. in the density of $Ni_{75}Fe_{25}$ nanoparticles in the seeding step) to favor the growth of one network over the other.[53] It is therefore possible to increase the likelihood of single-gyroid regions by restricting the amount of $Ni_{75}Fe_{25}$ deposited into the gyroid polymer template during constant-potential growth, via limiting the total charge supplied by the potentiostat. **Figure 3a** shows a double-gyroid nanoparticle from a sample deposited with a total charge of 20 mC, whereas in **Figure 3c** the sample was deposited with total charge of only 5 mC, showing a (111)-oriented nanoparticle containing a double-gyroid region and a single-gyroid region, allowing the properties of a single-gyroid network to be studied as well.

The magnetic state of the gyroid particles was studied by mapping the electron optical phase shift within and around the struts by off-axis EH measurements using an aberration-corrected transmission electron microscope operated at 300 kV.[54] The preparation of the gyroid samples as isolated small grains and the mechanical and electrical properties of the graphene oxide coatings on the grids helped to reduce background in the experiments. The sample was magnetized using the field (~1.4 T) of the objective lens of the microscope and the remanent state was recorded. By combining images taken with the sample magnetized in opposite directions, the phase shift from the sample could be separated into contributions from the mean inner potential (the volume average of the local electrostatic potentials) and from the magnetic phase shift induced by the in-

plane magnetic vector potential in the sample, as described in detail in the Supporting Information (**Figure S3**). The magnetic flux around the gyroids was then visualized by adding contours and colors showing the magnitude and direction of the in-plane magnetic field.

Figure 3a and **3b** display the mean inner potential contribution to the electron optical phase shift of the double-gyroid particle and the corresponding magnetic induction map, respectively. The external stray field around the gyroid is similar to that of a dipole aligned to the saturating field (H). Internally several flux-closed loops can also be identified which enclose as few as one unit cell, although identifying their chirality is complicated as the magnetic induction map is integrated through the thickness of several unit cells and both interpenetrating gyroid networks. However, the single-gyroid region in the particle in **Figure 3c** is only one unit cell thick, with the [111] direction normal to the substrate.

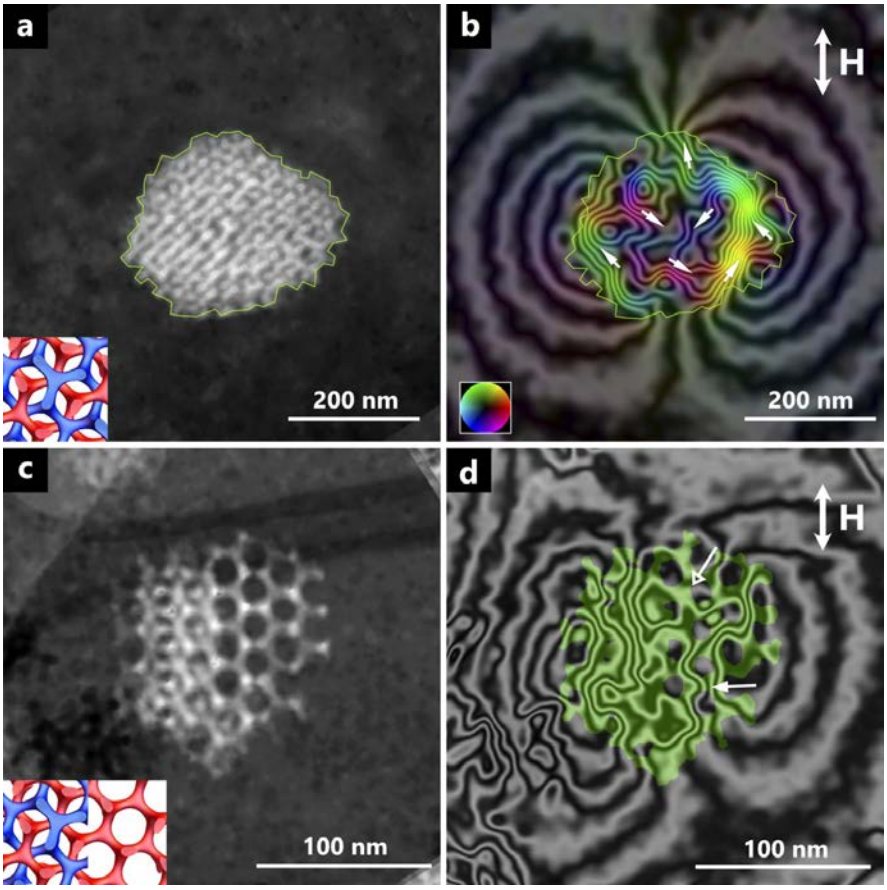

Figure 3. Magnetic imaging of Ni-Fe double- and single-gyroid structures. Insets show a few simulated unit cells of double-gyroids and mixed double-/single-gyroid structures, in which the two gyroid networks are highlighted in red and blue. (a, b) Mean inner potential and magnetic induction map of a double-gyroid nanoparticle. The double-headed arrows indicate the direction of the magnetic field (H) used to saturate the sample. The magnetic flux contour lines show the stray field around the nanoparticle. In the inner part the field density varies due to the random field directions (shown by the single-headed arrows). The contour of the nanoparticle is

generated from the mean inner potential contribution to the phase shift and depicted in (b). (c, d) Mean inner potential and the corresponding magnetic flux contour map of a nanoparticle with both double-gyroid and single-gyroid regions. In (d), the gyroid particle was masked, shaded with green color and then overlapped with the contour lines to show the field lines relative to the gyroid struts. Locations where flux contours cut across gyroid struts or encircle vertices are indicated with closed and open single-headed arrows, respectively. The contour spacing in both (c) and (d) is $2\pi/64$ radians.

In the single-gyroid region, the relationship between the structure and magnetization of the ferromagnetic gyroid becomes clearer (**Figure 3d**). The external stray field is still dipole-like, but the single-gyroid's remanent state is not a simple network of flux-closed loops. The flux contours largely follow the structure, but in some locations (highlighted in the figure) the flux lines cut directly across struts, suggesting that the magnetization is transverse to the strut axis. In other locations, the flux contours encircle certain vertices, possibly indicating that the magnetizations of the three constituent struts all point towards or all away from the vertex center. The magnetic phase shift φ_m across a single gyroid strut, as presented in **Figure 3d**, is measured experimentally to be in the range of 0.15 to 0.2 rad. Assuming a cylindrical permalloy structure, the predicted magnetic phase shift can be calculated from the expression $\varphi_m = \pi \cdot (e/\hbar) \cdot B_0 \cdot a^2$, where e is the elementary charge, $\hbar$ is the reduced Planck's constant, B_0 is the saturation magnetic induction (1 T for permalloy) and a is the radius of the cylinder. The magnetic phase shifts of permalloy cylinders with diameters of 11 and 12 nm are predicted to be 0.14 and 0.17 rad, respectively. The consistency with the experimentally measured values is encouraging.

Kommentiert [JL1]: Modified from "…indicating magnetization transverse to the strut axis" in response to referee's comment #2

Kommentiert [JL2]: Added to answer referee's comment #1

Off-axis EH experiments confirm that gyroids are ferromagnetic at room temperature and have a remanent state with a dipole stray field. However, as the recorded electron optical phase shift maps are 2D projections integrated through the gyroid unit cell thickness and the approach that we used to achieve magnetization switching cannot be verified to perfectly reverse the magnetic state in the sample, the 3D magnetization distribution cannot be recovered unambiguously. As magnetic field tomography[55] is not yet feasible for samples like the gyroid networks studied here, in order to interpret the off-axis EH images we employed finite-element micromagnetic simulations using the GPU-accelerated finite-element package TetraMag[56] to model the 3D magnetization. Details of the micromagnetic simulations are given in the Supporting Information. **Figure 4a** shows the magnetization configuration of a simulated Ni-Fe nanoparticle similar to that in **Figure 3c** divided into double-gyroid and single-gyroid regions with a 42 nm unit cell and a filling fraction of approximately 19%. The simulation mesh (4×5×1 unit cells) is oriented to show the (111) plane and shows the remanent state after relaxation of a randomly magnetized initial state. The color indicates the angle of the projected in-plane magnetization vector relative to $+x$ (the [$\bar{1}$10] direction), according to the color wheel. A subset of struts in the single-gyroid region has been decorated with arrows which identify the average in-plane magnetization direction. As expected, even this 2D projection of the full 3D magnetization pattern is extremely complex. By examining pairs of vertices, which share one of their struts, two situations can be distinguished. In the first (**Figure 4b**), the strut connecting the two vertices has nearly uniform magnetization along its axis. The remaining two struts in each of the two vertices also adopt nearly uniform magnetizations, leading to a "1-in, 2-out" (and vice versa) configuration at each vertex.

Kommentiert [JL3]: Added to answer referee's comment #2

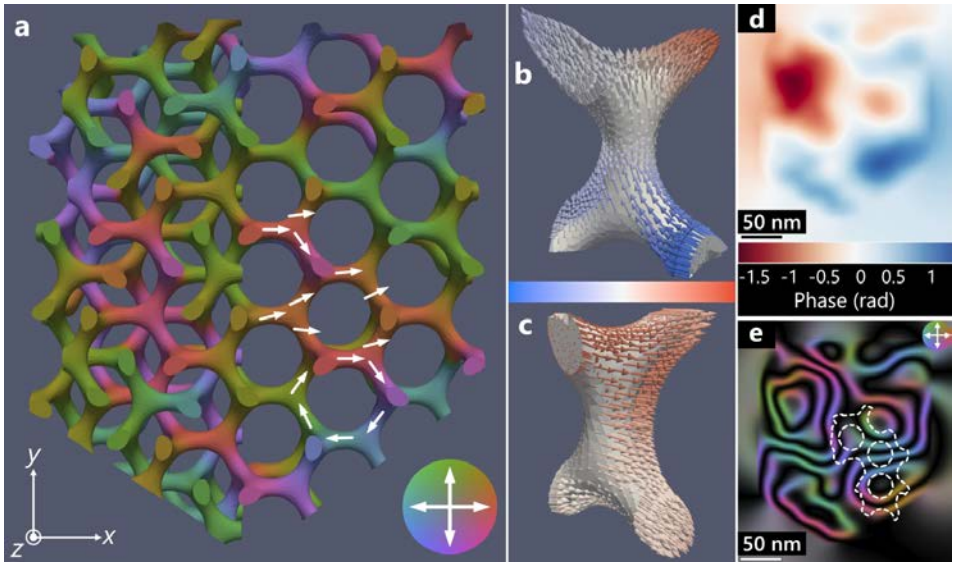

Figure 4. Micromagnetic simulations of gyroid structures. (a) Micromagnetic configuration of model Ni-Fe gyroid particle after relaxation from a randomly magnetized state, obtained using the TetraMag finite-element package[56] as described in the Supporting Information. The unit cell length was set to 42 nm. The color wheel shows the direction of the in-plane magnetization vector. White single-headed arrows show the average magnetization direction of a subset of struts. (b, c) Magnified views of two common types of vertex-pair magnetization configurations, with colored arrows indicating the directions of the local magnetization vector. The horizontal color bar between the two images indicates the relative direction of the magnetization to the line joining the two vertices (vertical along the page). (d) 2D-projected magnetic phase shift of the simulated Ni-Fe gyroid nanoparticle in (a) calculated by projecting the in-plane magnetization components (M_x and M_y) along the *z*-axis (the beam direction in the experimental off-axis EH images) and (e) the resulting magnetic induction map, generated from the phase map by adding a cosine to the phase change. Dashes mark the same subset of struts decorated with arrows in (a).

In the second situation (**Figure 4c**), the magnetization of the connecting strut is still uniform but is now mostly transverse to its axis, twisting in space to allow the magnetizations of the pairs of remaining struts at the two vertices to point in the same direction. This behavior explains why flux lines cut across gyroid struts in some locations in the magnetic induction map in **Figure 3d**, although these configurations seem to occur more frequently in the (ideal) micromagnetic simulation. Such configurations permit the gyroid to relieve frustration by a completely different mechanism than is seen in 2D artificial spin ice systems, and are only allowed by the 3D nature of the struts and the chiral twist between vertices.

In the double-gyroid region at the left of **Figure 4a**, the presence of magnetostatic interactions between the two gyroid sub-networks may be discerned. When adjacent, parallel struts in the two sub-networks are both magnetized along their mutual axis (the first situation described above), the struts attempt to adopt alternating magnetization directions. However, the competing demands of magnetization continuity at the vertices within each sub-network seem to overcome the magnetostatic interactions between sub-networks. It also appears that struts with transverse magnetization (the second situation described above) are less common within the body of the double-gyroid region.

To support the conclusions drawn from the micromagnetic simulations, we use the obtained 3D magnetization distribution shown in **Figure 4a** to calculate the 2D projection of the resulting magnetic phase shifts (**Figure 4d**), from which magnetic induction maps (**Figure 4e**) can be derived using the same method used to produce the experimental maps. Good qualitative agreement is obtained between the calculated result from the simulated micromagnetic configurations in **Figure 4e** and the magnetic induction images obtained from the off-axis EH measurements in **Figure 3**. Features such as flux lines encircling vertices or cutting across struts

are reproduced in the simulations. We note that we have performed a large number of simulations employing various initial conditions, including both different randomized states and saturated conditions with the field applied along directions encompassing the full angular range (both in-plane and out-of-plane). In all cases, a dipolar stray field pattern appears, but no unique well-defined equilibrium microstate is observed.

The appearance of the gyroid's {111} planes invites comparison to honeycomb and kagomé artificial spin ices,[26,57–60] in which planar Ising-like nanomagnets form a 2D network of Y-shaped vertices. However, it is prudent to recall that the hexagonal structures forming the gyroid's {111} planes are sections of a helix viewed end-on, rather than a planar lattice. Direct correlations to 2D artificial spin ices must therefore be drawn with caution.

In summary, we have produced double-gyroid and single-gyroid nanostructures from electrodeposited $Ni_{75}Fe_{25}$ with unit cells below 50 nm and obtained maps of the magnetic induction that can be related to the magnetization of gyroid struts and vertices. Simulations indicate complex zero-field magnetization patterns, constructed from pairs of interacting vertices which tend to adopt one of two preferential configurations. The experimental measurements and simulations indicate that the 3D gyroid network permits many equivalent magnetization configurations, which may be prospective for applications such as reservoir computing[61] where a nanoscale system with high interconnectivity and a large number of possible stable states is advantageous. For gyroids with slightly larger unit cells and thicker struts which favor the formation of more confined domain walls, the non-uniform curvature of the struts creates a periodic network of natural pinning sites which could be exploited to create a "reset" state. The characteristic dimensions of the magnetic gyroids shown in this work highlight their potential as 3D magnonic crystals,[36] though further work will be required to evaluate magnetization dynamics and spin-wave propagation, including

the prospect of the same non-reciprocal transmission observed for light in gyroid photonic structures.[11,20,62] Although spin and charge transport properties in gyroids remain to be investigated, we expect our results to spur the application of nanoscale magnetic gyroids to fields such as spintronics and take a first step towards 3D nanoscale magnetic metamaterials displaying new emergent phenomena.

ASSOCIATED CONTENT

Supporting Information.

High-symmetry directions of the gyroid structure; additional details about (a) block co-polymer templating and (b) electrodeposition of Ni-Fe gyroids on Au-coated Si, FTO-coated glass and TEM grids, (c) analysis procedure of acquired electron holograms and extraction of phase and induction maps, with magnetic induction map of a large Ni-Fe double-gyroid "nanowire", (d) magnetization switching consistency and side-by-side comparison of experimental and simulated induction maps of single/double-gyroid nanoparticles, and (e) micromagnetic simulation parameters.

The following files are available free of charge.

brief description (file type, i.e., PDF)

Kommentiert [JL4]: Added in response to reviewer comments #2 and #3

AUTHOR INFORMATION

Corresponding Author

*Justin Llandro (justin@riec.tohoku.ac.jp)

Present Addresses

‡Lightpoint Medical Ltd., Misbourne Works, Waterside, Chesham HP5 1PE, UK.

§Papierfabrik Louisenthal GmbH, 83701 Gmund am Tegernsee, Germany.

Notes

The authors declare that they have no competing financial interests.

ACKNOWLEDGMENT

J.L. thanks Tomasz Dietl for helpful discussions and acknowledges GP-Spin at Tohoku University for support and also postdoctoral funding from EPSRC grant EP/J00412X/1 "Mapping Spin Polarisation in Quasi- One-Dimensional Channels". This project has received funding from the European Research Council (ERC) under the grant agreement 320832, the European Union's Horizon 2020 research and innovation programme under grant agreement 856538 and from the Japan Society for the Promotion of Science (JSPS) under Kakenhi Grant number 19H05622. M.R.J.S. acknowledges funding from Nokia Research Centre Cambridge. U.S. acknowledges funding from the Adolphe Merkle Foundation. J. L and A.K. acknowledge Naëmi Leo for her helpful suggestions on the manuscript.

ABBREVIATIONS

EH, electron holography; ALD, atomic layer deposition; FTO, fluorine-doped tin oxide; SAXS, small-angle X-ray scattering; SEM, scanning electron microscopy; TEM, transmission electron microscopy; PFS, poly(4-fluorostyrene); PLA, poly(lactic acid); VSM, vibrating sample magnetometry; EDX, energy-dispersive X-ray spectroscopy; DMI, Dzyaloshinskii-Moriya interaction

REFERENCES

(1) Luzzati, V.; Spegt, P. A. Polymorphism of Lipids. *Nature* **1967**, *215*, 701–704. https://doi.org/10.1038/2171028a0.

(2) Schoen, A. H. Infinite Periodic Minimal Surfaces without Self-Intersections. *Nasa Tech. Note D-5541* **1970**, 92.

(3) Han, L.; Che, S. An Overview of Materials with Triply Periodic Minimal Surfaces and Related Geometry: From Biological Structures to Self-Assembled Systems. *Adv. Mater.* **2018**, *30* (17), 1705708. https://doi.org/10.1002/adma.201705708.

(4) Michielsen, K.; Stavenga, D. . Gyroid Cuticular Structures in Butterfly Wing Scales: Biological Photonic Crystals. *J. R. Soc. Interface* **2008**, *5* (18), 85–94. https://doi.org/10.1098/rsif.2007.1065.

(5) Michielsen, K.; De Raedt, H.; Stavenga, D. G. Reflectivity of the Gyroid Biophotonic Crystals in the Ventral Wing Scales of the Green Hairstreak Butterfly, Callophrys Rubi. *J. R. Soc. Interface* **2010**, *7* (October 2009), 765–771. https://doi.org/10.1098/rsif.2009.0352.

(6) Saranathan, V.; Osuji, C. O.; Mochrie, S. G. J.; Noh, H.; Narayanan, S.; Sandy, A.; Dufresne, E. R.; Prum, R. O. Structure, Function, and Self-Assembly of Single Network Gyroid (I4132) Photonic Crystals in Butterfly Wing Scales. *Proc. Natl. Acad. Sci.* **2010**, *107* (26), 11676–11681. https://doi.org/10.1073/pnas.0909616107.

(7) Schröder-Turk, G. E.; Wickham, S.; Averdunk, H.; Brink, F.; Fitz Gerald, J. D.; Poladian, L.; Large, M. C. J.; Hyde, S. T. The Chiral Structure of Porous Chitin within the Wing-Scales of Callophrys Rubi. *J. Struct. Biol.* **2011**, *174* (2), 290–295. https://doi.org/10.1016/j.jsb.2011.01.004.

(8) Schroeder, T. B. H.; Houghtaling, J.; Wilts, B. D.; Mayer, M. It's Not a Bug, It's a Feature:

Functional Materials in Insects. *Adv. Mater.* **2018**, *30* (19), 1705322. https://doi.org/10.1002/adma.201705322.

(9) Yan, C.; Hao, L.; Hussein, A.; Raymont, D. Evaluations of Cellular Lattice Structures Manufactured Using Selective Laser Melting. *Int. J. Mach. Tools Manuf.* **2012**, *62*, 32–38. https://doi.org/10.1016/j.ijmachtools.2012.06.002.

(10) Yánez, A.; Herrera, A.; Martel, O.; Monopoli, D.; Afonso, H. Compressive Behaviour of Gyroid Lattice Structures for Human Cancellous Bone Implant Applications. *Mater. Sci. Eng. C* **2016**, *68*, 445–448. https://doi.org/10.1016/j.msec.2016.06.016.

(11) Turner, M. D.; Saba, M.; Zhang, Q.; Cumming, B. P.; Schröder-Turk, G. E.; Gu, M. Miniature Chiral Beamsplitter Based on Gyroid Photonic Crystals. *Nat. Photonics* **2013**, *7* (10), 801–805. https://doi.org/10.1038/nphoton.2013.233.

(12) Gan, Z.; Turner, M. D.; Gu, M. Biomimetic Gyroid Nanostructures Exceeding Their Natural Origins. *Sci. Adv.* **2016**, *2* (5), 1600084. https://doi.org/10.1126/sciadv.1600084.

(13) Armatas, G. S.; Kanatzidis, M. G. Mesostructured Germanium with Cubic Pore Symmetry. *Nature* **2006**, *441* (7097), 1122–1125. https://doi.org/10.1038/nature04833.

(14) Kresge, C. T.; Leonowicz, M. E.; Roth, W. J.; Vartuli, J. C.; Beck, J. S. Ordered Mesoporous Molecular Sieves Synthesized by a Liquid-Crystal Template Mechanism. *Nature* **1992**, *359* (6397), 710–712. https://doi.org/10.1038/359710a0.

(15) Hajduk, D. A.; Harper, P. E.; Gruner, S. M.; Honeker, C. C.; Kim, G.; Thomas, E. L.; Fetters, L. J. The Gyroid- a New Equilibrium Morphology in Weakly Segregated Diblock Copolymers. *Macromolecules* **1994**, *27*, 4063–4075. https://doi.org/10.1021/ma00093a006.

(16) Kim, J. K.; Yang, S. Y.; Lee, Y.; Kim, Y. Functional Nanomaterials Based on Block

Copolymer Self-Assembly. *Prog. Polym. Sci.* **2010**, *35* (11), 1325–1349. https://doi.org/10.1016/j.progpolymsci.2010.06.002.

(17) Bai, W.; Hannon, A. F.; Gotrik, K. W.; Choi, H. K.; Aissou, K.; Liontos, G.; Ntetsikas, K.; Alexander-Katz, A.; Avgeropoulos, A.; Ross, C. A. Thin Film Morphologies of Bulk-Gyroid Polystyrene- Block -Polydimethylsiloxane under Solvent Vapor Annealing. *Macromolecules* **2014**, *47* (17), 6000–6008. https://doi.org/10.1021/ma501293n.

(18) Hsueh, H.; Yao, C.; Ho, R. Well-Ordered Nanohybrids and Nanoporous Materials from Gyroid Block Copolymer Templates. *Chem. Soc. Rev.* **2015**, *44* (7), 1974–2018. https://doi.org/10.1039/C4CS00424H.

(19) Vignolini, S.; Yufa, N. A.; Cunha, P. S.; Guldin, S.; Rushkin, I.; Stefik, M.; Hur, K.; Wiesner, U.; Baumberg, J. J.; Steiner, U. A 3D Optical Metamaterial Made by Self-Assembly. *Adv. Mater.* **2012**, *24* (10), OP23–OP27. https://doi.org/10.1002/adma.201103610.

(20) Dolan, J. A.; Wilts, B. D.; Vignolini, S.; Baumberg, J. J.; Steiner, U.; Wilkinson, T. D. Optical Properties of Gyroid Structured Materials: From Photonic Crystals to Metamaterials. *Adv. Opt. Mater.* **2015**, *3* (1), 12–32. https://doi.org/10.1002/adom.201400333.

(21) Farah, P.; Demetriadou, A.; Salvatore, S.; Vignolini, S.; Stefik, M.; Wiesner, U.; Hess, O.; Steiner, U.; Valev, V. K.; Baumberg, J. J. Ultrafast Nonlinear Response of Gold Gyroid Three-Dimensional Metamaterials. *Phys. Rev. Appl.* **2014**, *2* (4), 044002. https://doi.org/10.1103/PhysRevApplied.2.044002.

(22) Lu, L.; Fu, L.; Joannopoulos, J. D.; Soljačić, M. Weyl Points and Line Nodes in Gyroid Photonic Crystals. *Nat. Photonics* **2013**, *7* (4), 294–299.

https://doi.org/10.1038/nphoton.2013.42.

(23) Lu, L.; Wang, Z.; Ye, D.; Ran, L.; Fu, L.; Joannopoulos, J. D.; Soljačić, M. Experimental Observation of Weyl Points. *Science* **2015**, *349* (6248), 622–624. https://doi.org/10.1126/science.aaa9273.

(24) Hyde, S. T.; O'Keeffe, M.; Proserpio, D. M. A Short History of an Elusive yet Ubiquitous Structure in Chemistry, Materials, and Mathematics. *Angew. Chemie - Int. Ed.* **2008**, *47* (42), 7996–8000. https://doi.org/10.1002/anie.200801519.

(25) Mizuno, A.; Shuku, Y.; Awaga, K. Recent Developments in Molecular Spin Gyroid Research. *Bull. Chem. Soc. Jpn.* **2019**, *92* (6), 1068–1093. https://doi.org/10.1246/bcsj.20190033.

(26) Skjærvø, S. H.; Marrows, C. H.; Stamps, R. L.; Heyderman, L. J. Advances in Artificial Spin Ice. *Nat. Rev. Phys.* **2020**, *2*, 13–28. https://doi.org/10.1038/s42254-019-0118-3.

(27) Nisoli, C.; Kapaklis, V.; Schiffer, P. Deliberate Exotic Magnetism via Frustration and Topology. *Nat. Phys.* **2017**, *13* (March), 200–203.

(28) Streubel, R.; Fischer, P.; Kronast, F.; Kravchuk, V. P.; Sheka, D. D.; Gaididei, Y.; Schmidt, O. G.; Makarov, D. Magnetism in Curved Geometries. *J. Phys. D. Appl. Phys.* **2016**, *49* (36), 363001. https://doi.org/10.1088/0022-3727/49/36/363001.

(29) Fernández-Pacheco, A.; Streubel, R.; Fruchart, O.; Hertel, R.; Fischer, P.; Cowburn, R. P. Three-Dimensional Nanomagnetism. *Nat. Commun.* **2017**, *8*, 15756. https://doi.org/10.1038/ncomms15756.

(30) Sander, D.; Valenzuela, S. O.; Makarov, D.; Marrows, C. H.; Fullerton, E. E.; Fischer, P.; McCord, J.; Vavassori, P.; Mangin, S.; Pirro, P.; et al. The 2017 Magnetism Roadmap. *J. Phys. D. Appl. Phys.* **2017**, *50* (36), 363001. https://doi.org/10.1088/1361-6463/aa81a1.

(31) Gaididei, Y.; Kravchuk, V. P.; Sheka, D. D. Curvature Effects in Thin Magnetic Shells. *Phys. Rev. Lett.* **2014**, *112* (25), 257203. https://doi.org/10.1103/PhysRevLett.112.257203.

(32) Pylypovskyi, O. V.; Kravchuk, V. P.; Sheka, D. D.; Makarov, D.; Schmidt, O. G.; Gaididei, Y. Coupling of Chiralities in Spin and Physical Spaces: The Möbius Ring as a Case Study. *Phys. Rev. Lett.* **2015**, *114* (19), 197204. https://doi.org/10.1103/PhysRevLett.114.197204.

(33) Otálora, J. A.; Yan, M.; Schultheiss, H.; Hertel, R.; Kákay, A. Curvature-Induced Asymmetric Spin-Wave Dispersion. *Phys. Rev. Lett.* **2016**, *117* (22), 227203. https://doi.org/10.1103/PhysRevLett.117.227203.

(34) Volkov, O. M.; Sheka, D. D.; Gaididei, Y.; Kravchuk, V. P.; Rößler, U. K.; Fassbender, J.; Makarov, D. Mesoscale Dzyaloshinskii-Moriya Interaction: Geometrical Tailoring of the Magnetochirality. *Sci. Rep.* **2018**, *8* (1), 866. https://doi.org/10.1038/s41598-017-18835-4.

(35) Volkov, O. M.; Rößler, U. K.; Fassbender, J.; Makarov, D. Concept of Artificial Magnetoelectric Materials via Geometrically Controlling Curvilinear Helimagnets. *J. Phys. D. Appl. Phys.* **2019**, *52* (34), 345001. https://doi.org/10.1088/1361-6463/ab2368.

(36) Chumak, A. V.; Serga, A. A.; Hillebrands, B. Magnonic Crystals for Data Processing. *J. Phys. D. Appl. Phys.* **2017**, *50* (24), 244001. https://doi.org/10.1088/1361-6463/aa6a65.

(37) Hopfield, J. J. Neural Networks and Physical Systems with Emergent Collective Computational Abilities. *Proc. Natl. Acad. Sci.* **1982**, *79* (8), 2554–2558. https://doi.org/10.1073/pnas.79.8.2554.

(38) Hsueh, H.-Y.; Huang, Y.-C.; Ho, R.-M.; Lai, C.-H.; Makida, T.; Hasegawa, H. Nanoporous Gyroid Nickel from Block Copolymer Templates via Electroless Plating. *Adv. Mater.* **2011**, *23* (27), 3041–3046. https://doi.org/10.1002/adma.201100883.

(39) Almeida, T. P.; Kasama, T.; Muxworthy, A. R.; Williams, W.; Nagy, L.; Hansen, T. W.;

Brown, P. D.; Dunin-Borkowski, R. E. Visualized Effect of Oxidation on Magnetic Recording Fidelity in Pseudo-Single-Domain Magnetite Particles. *Nat. Commun.* **2014**, *5* (1), 5154. https://doi.org/10.1038/ncomms6154.

(40) Biziere, N.; Gatel, C.; Lassalle-Balier, R.; Clochard, M. C.; Wegrowe, J. E.; Snoeck, E. Imaging the Fine Structure of a Magnetic Domain Wall in a Ni Nanocylinder. *Nano Lett.* **2013**, *13* (5), 2053–2057. https://doi.org/10.1021/nl400317j.

(41) Phatak, C.; Liu, Y.; Gulsoy, E. B.; Schmidt, D.; Franke-Schubert, E.; Petford-Long, A. Visualization of the Magnetic Structure of Sculpted Three-Dimensional Cobalt Nanospirals. *Nano Lett.* **2014**, *14* (2), 759–764. https://doi.org/10.1021/nl404071u.

(42) Jin, C.; Li, Z.-A.; Kovács, A.; Caron, J.; Zheng, F.; Rybakov, F. N.; Kiselev, N. S.; Du, H.; Blügel, S.; Tian, M.; et al. Control of Morphology and Formation of Highly Geometrically Confined Magnetic Skyrmions. *Nat. Commun.* **2017**, *8* (1), 15569. https://doi.org/10.1038/ncomms15569.

(43) Midgley, P. A.; Dunin-Borkowski, R. E. Electron Tomography and Holography in Materials Science. *Nat. Mater.* **2009**, *8* (4), 271–280. https://doi.org/10.1038/nmat2406.

(44) Kovács, A.; Dunin-Borkowski, R. E. Magnetic Imaging of Nanostructures Using Off-Axis Electron Holography. In *Handbook of Magnetic Materials 27*; Brück, E., Ed.; North-Holland: Amsterdam, **2018**; pp 59–153. https://doi.org/10.1016/bs.hmm.2018.09.001.

(45) Phatak, C.; Petford-Long, A. K.; De Graef, M. Recent Advances in Lorentz Microscopy. *Curr. Opin. Solid State Mater. Sci.* **2016**, *20* (2), 107–114. https://doi.org/10.1016/j.cossms.2016.01.002.

(46) Ross, C. A.; Berggren, K. K.; Cheng, J. Y.; Jung, Y. S.; Chang, J. Three-Dimensional Nanofabrication by Block Copolymer Self-Assembly. *Adv. Mater.* **2014**, *26* (25), 4386–

4396. https://doi.org/10.1002/adma.201400386.

(47) She, M.; Lo, T.; Ho, R. Controlled Ordering of Block Copolymer Gyroid Thin Films by Solvent Annealing. *Macromolecules* **2014**, *47* (1), 175–182. https://doi.org/10.1021/ma402187j.

(48) Dehmel, R.; Dolan, J. A.; Gu, Y.; Wiesner, U.; Wilkinson, T. D.; Baumberg, J. J.; Steiner, U.; Wilts, B. D.; Gunkel, I. Optical Imaging of Large Gyroid Grains in Block Copolymer Templates by Confined Crystallization. *Macromolecules* **2017**, *50* (16), 6255–6262. https://doi.org/10.1021/acs.macromol.7b01528.

(49) Dolan, J. A.; Korzeb, K.; Dehmel, R.; Gödel, K. C.; Stefik, M.; Wiesner, U.; Wilkinson, T. D.; Baumberg, J. J.; Wilts, B. D.; Steiner, U.; et al. Controlling Self-Assembly in Gyroid Terpolymer Films By Solvent Vapor Annealing. *Small* **2018**, *1802401*, 1802401. https://doi.org/10.1002/smll.201802401.

(50) Scherer, M. R. J.; Cunha, P. M. S.; Steiner, U. Labyrinth-Induced Faceted Electrochemical Growth. *Adv. Mater.* **2014**, *26* (15), 2403–2407. https://doi.org/10.1002/adma.201305074.

(51) Scherer, M. R. J.; Steiner, U. Efficient Electrochromic Devices Made from 3D Nanotubular Gyroid Networks. *Nano Lett.* **2013**, *13* (7), 3005–3010. https://doi.org/10.1021/nl303833h.

(52) Hertel, R.; Kákay, A. Analytic Form of Transverse Head-to-Head Domain Walls in Thin Cylindrical Wires. *J. Magn. Magn. Mater.* **2015**, *379*, 45–49. https://doi.org/10.1016/j.jmmm.2014.11.073.

(53) Yang, K.-C.; Yao, C.-T.; Huang, L.-Y.; Tsai, J.-C.; Hung, W.-S.; Hsueh, H.-Y.; Ho, R.-M. Single Gyroid-Structured Metallic Nanoporous Spheres Fabricated from Double Gyroid-Forming Block Copolymers via Templated Electroless Plating. *NPG Asia Mater.* **2019**, *11* (1), 9. https://doi.org/10.1038/s41427-019-0108-z.

(54) Boothroyd, C.; Kovács, A.; Tillmann, K. FEI Titan G2 60-300 HOLO. *J. large-scale Res. Facil.* **2016**, *2*, A44. https://doi.org/10.17815/jlsrf-2-70.

(55) Wolf, D.; Biziere, N.; Sturm, S.; Reyes, D.; Wade, T.; Niermann, T.; Krehl, J.; Warot-Fonrose, B.; Büchner, B.; Snoeck, E.; et al. Holographic Vector Field Electron Tomography of Three-Dimensional Nanomagnets. *Commun. Phys.* **2019**, *2* (1), 87. https://doi.org/10.1038/s42005-019-0187-8.

(56) Kákay, A.; Westphal, E.; Hertel, R. Speedup of FEM Micromagnetic Simulations with Graphical Processing Units. *IEEE Trans. Magn.* **2010**, *46* (6), 2303–2306. https://doi.org/10.1109/TMAG.2010.2048016.

(57) Branford, W. R.; Ladak, S.; Read, D. E.; Zeissler, K.; Cohen, L. F. Emerging Chirality in Artificial Spin Ice. *Science* **2012**, *335* (6076), 1597–1600. https://doi.org/10.1126/science.1211379.

(58) Zeissler, K.; Chadha, M.; Lovell, E.; Cohen, L. F.; Branford, W. R. Low Temperature and High Field Regimes of Connected Kagome Artificial Spin Ice: The Role of Domain Wall Topology. *Sci. Rep.* **2016**, *6* (1), 30218. https://doi.org/10.1038/srep30218.

(59) Le, B. L.; Park, J.; Sklenar, J.; Chern, G.-W.; Nisoli, C.; Watts, J. D.; Manno, M.; Rench, D. W.; Samarth, N.; Leighton, C.; et al. Understanding Magnetotransport Signatures in Networks of Connected Permalloy Nanowires. *Phys. Rev. B* **2017**, *95* (6), 060405. https://doi.org/10.1103/PhysRevB.95.060405.

(60) Summers, B.; Debeer-Schmitt, L.; Dahal, A.; Glavic, A.; Kampschroeder, P.; Gunasekera, J.; Singh, D. K. Temperature-Dependent Magnetism in Artificial Honeycomb Lattice of Connected Elements. *Phys. Rev. B* **2018**, *97* (1), 014401. https://doi.org/10.1103/PhysRevB.97.014401.

(61) Tanaka, G.; Yamane, T.; Héroux, J. B.; Nakane, R.; Kanazawa, N.; Takeda, S.; Numata, H.; Nakano, D.; Hirose, A. Recent Advances in Physical Reservoir Computing: A Review. *Neural Networks* **2019**, *115*, 100–123. https://doi.org/ 10.1016/j.neunet.2019.03.005.

(62) Wu, L.; Zhang, W.; Zhang, D. Engineering Gyroid-Structured Functional Materials via Templates Discovered in Nature and in the Lab. *Small* **2015**, *11* (38), 5004–5022. https://doi.org/10.1002/smll.201500812.

For Table of Contents Only